ORIGINAL PAPER

Physical Model Tests on the Effect of Anchoring on the Splitting Failure of Deep Large-Scale Underground Rock Cavern

Guangyuan Yu · Qiangyong Zhang · Fan Li · Lei Cheng · Xin Guo

Abstract A set of splitting cracks often occur in the high side wall of the deep underground hydropower station due to the excavation-induced unloading during the construction period, which causes great risk to the safety of the cavern. In this paper, taking the Pubugou Hydropower Station as the engineering background, we perform true three-dimensional geomechanical model tests to investigate the effect of anchoring on restraining splitting failure. The evolutions of deformation and stress in the surrounding rock and the internal force of support structure are monitored. The test results of unsupported model reveal that the displacement and stress of the surrounding rock at the side wall and haunch show non-monotonic fluctuations after excavation. In the supported model, no splitting failure occurs and the displacement is much smaller compared with the unsupported model. During the layered excavation of the high side wall cavern, the stress concentration area moves to the bottom of the cavern in the supported model. After excavation, the displacement and radial stress present a monotonous change in the supported model, but within the range of 1.5 times cavern span, the tangential stress presents a fluctuating variation that first increases and then decreases. It can be seen that the anchorage support can effectively limit the

splitting failure and improve the distribution of stress in the surrounding rock. These results provide basis and reference for in-depth analysis of the excavation stability of high-side wall caverns under high ground stress and optimization of the cavern support design.

Keywords Geo-mechanical model test · Splitting failure · Large-scale underground cavern · Anchorage support

1 Introduction

In southwest China, a large number of underground powerhouse projects have been constructed under high in-situ stress. In the area with high ground stress, a large number of splitting fractures often appear in the high side wall of the underground powerhouse, forming a large group of parallel cracks with vertical distribution (Hibino et al. 1995). Splitting failure is defined as spalling or slabbing damage (Du et al. 2016; Luo et al. 2019). Although the name is not exactly the same, the essence is that under high in-situ stress, multiple sets of vertical cracks are formed approximately parallel to the side wall, causing stratified failure of surrounding rocks. Splitting failure of high side wall cavern is an important factor affecting the safety of underground cavern construction, which has been the focus of recent researches.

G. Yu (✉) · Q. Zhang · F. Li · L. Cheng · X. Guo
Geotechnical and Structural Engineering Research Center, Shandong University, Jinan, China
e-mail: guangyuan.yu@qq.com

By means of numerical simulation (Tang et al. 2005; Guo et al. 2010), field observation (Hibino 2001; Yoshida et al. 2004) and physical model test (Gong et al. 2019), abundant studies have been carried out with the focus on the spalling process (Liu et al. 2017), mechanical mechanism of splitting failure (Li et al. 2017), prediction of the splitting depth (Zhu et al. 2014) and estimation of the splitting failure zone (Li et al. 2014). At present, most researches on splitting failure are mainly based on the plane strain, and the excavation unloading under the true three-dimensional high ground stress is not considered.

Regarding the support system of underground caverns, plenty of work has been carried out through site observation (Xiao et al. 2018; Qian et al. 2018), numerical simulation (Malmgren et al. 2008; Prasad et al. 2013; Li et al. 2016; Behnia et al. 2018), laboratory tests (Zhou et al. 2015), and theoretical analysis (Chen et al. 2018). In the aspect of numerical simulation, finite element method, finite difference method and discrete element method are widely employed. Boon et al. (2015) illustrated a systematic approach of using the distinct element method (DEM) to determine the main parameters of the support and evaluate the support effect. Liu et al. (2018) provided a sound support design for a large-scale underground water-sealed oil storage facility in China using both empirical rock mass classification and finite difference method. Gao et al (2019) proposed an equivalent simulation method for the bolted anisotropic rock mass by finite element method.

For the theoretical research of underground cavern support, Fahimifar et al. (2005) derived the relationships between grouted rock bolts and rock mass with consideration of a non-linear strength criterion for rock mass, two material behavior models and rock-support interaction concepts. Li et al. (2015) developed a theoretical model concerning the behavior of a single grouted cable bolt and performed a parametric investigation on bolt pretension, joint friction angle, concrete strength and bolt installation angle.

Geo-mechanical model test is a very effective method in the study of underground cavern support, which can not only simulate the excavation, but also simulate the interaction between support and surrounding rock (Zhu et al. 2010; Zhang et al. 2020). Zhang et al. (2019a, b) carried out a true three-dimensional geo-mechanical model test on a deep diversion tunnel passing through a weak fault and discussed the evolution and distribution of the stress and displacement, as well as the proportion of loads taken by surrounding rock and support system.

The above-mentioned studies have made a significant contribution to the correct understanding of splitting failure. Moreover, many researchers have done substantial studies on the support control of surrounding rock. However, few researches are reported on the effect of anchoring on splitting failure in deep caverns with high side wall. So far, the support anchorage effect on splitting failure is mainly studied through small-size rock specimens. The similarity between model and prototype and the supporting effect of systematic rockbolts are not considered in the tests on small specimens.

In this paper, taking the main powerhouse of Pubugou Hydropower Station in China as the engineering background, we have carried out two true three-dimensional geo-mechanical model tests to examine the anchoring effect of rock bolts and pre-stressed anchored cable on splitting failure. In specific, the evolution of the stress and displacement in surrounding rock, as well as, the variation of axial force of bolts and cables are revealed. The findings are expected to provide references for evaluating the surrounding rock mass stability and anchorage effect on splitting failure of large-scale underground cavern under high geo-stress.

2 Project Background

Pubugou Hydropower Station is located in the middle reaches of Dadu River in the west of Sichuan province, China. The power plant is located on the left bank. The plant is equipped with six hydro-turbines and the installed capacity of the power plant is 3300 MW. It is the largest installed power plant in the 22-stage planning cascade of Dadu River and the largest power plant in Sichuan Province. During the construction of the main powerhouse, a number of approximately parallel splitting cracks appear at the side wall, with the maximum width up to 20 mm.

The depth of the underground powerhouse group is 200–360 m. The surrounding rock is composed of breezed-fresh medium-coarse granulated granite, which is hard and integrated. The uniaxial compressive strength of the rock is generally above 100 MPa. There are no large faults in the plant site area. Dolerite

veins, fracture dense zone and small fault zone exist locally. The width of these fracture zones is mostly less than 20 cm. On the whole, the quality of surrounding rock is good and the rock mass is relatively intact. A large number of studies have proved that rock veins (Shang 2020) and faults (Ma et al. 2020) have a significant influence on the stability and mechanical characteristics of surrounding rock, nevertheless we do not consider discontinuities such as faults and fracture zones as the main factors in the model test. This is mainly because we believe that the main factors affecting surrounding rock stability in this project and splitting failure are the high ground stress environment and the special structure form of the high sidewall cavern. The scale of the main powerhouse is 208.6 m × 26.80 m × 70.10 m (length × width × height), and the axial direction of the main powerhouse is N45° E. The in-situ stress measurement results indicate that the horizontal stress is 15.25–27.01 MPa and the vertical stress is 8.11–17.96 MPa. The maximum principal stress is 21.1–27.3 MPa and its orientation is N54°–84°E. The angle between the maximum principal stress direction and the longitudinal axis of the cavern is 12°–42°.

3 Construction of the Geo-mechanical Model

We carried out two model tests to study the effect of anchoring on the splitting failure of underground cavern with high side wall. The two model tests were subjected to the same loading condition (Fig. 9a). The true 3D loading, which was calculated from the in-situ stress (σ1 = 27.30 MPa, σ2 = 16.16 MPa and σ3 = 15.25 MPa) following the similarity principles, was applied onto the model by hydraulic loading system. The same analogue materials of surrounding rock and model test system including the loading equipment, monitoring equipment and excavation equipment were used in the two model tests. The first model test was performed to reproduce the splitting failure, then the second model test was implemented with rock bolt and pre-stressed anchor cable support system to analyze the anchoring effect. Due to the limitation of the test device, the installing technology and size of the model cavern, the rock bolt and pre-stressed anchor cable were installed by the pre-embedded method. The construction and excavation processes were generally the same for the two tests,

despite that one more step of embedding rock bolts and pre-stressed anchor cables added in the second test. Also, the monitoring section of rock bolts and pre-stressed anchor cables was added.

3.1 Similarity Principles

The similarity principle of geomechanical model test means that the physical phenomena reproduced by the model should be similar to that of the engineering prototype, that is, the mechanical properties, geometry and stress characteristics of the model should follow certain rules and meet the similarity (Fumagalli et al. 1973).

According to the equilibrium equation, geometric equation, constitutive equation, stress boundary condition and displacement boundary condition of prototype and model, the similar conditions of geomechanical model test are established (Zhang et al. 2008). In the following formula, the parameters with the subscript P are the prototype parameters, and the parameters with the subscript M represent the model parameters.

Based on the equilibrium equation, the similar conditions are established as follows:

$$\frac{C_\gamma C_L}{C_\sigma} = 1 \qquad (1)$$

where L represents the length, σ represents the stress, γ represents the unit weight. $C_L = L_P/L_M$ is the geometric similarity ratio, $C_\sigma = \sigma_P/\sigma_M$ is the stress similarity ratio, $C_\gamma = \gamma_P/\gamma_M$ is the unit weight similarity ratio;

Based on the geometric equation, the similarity conditions are established as follows:

$$\frac{C_\varepsilon C_L}{C_\delta} = 1 \qquad (2)$$

where ε represents the strain, δ represents the displacement. $C_\varepsilon = \varepsilon_P/\varepsilon_M$ is the strain similarity ratio, $C_\delta = \delta_P/\delta_M$ is the displacement similarity ratio;

Based on the constitutive equation, the similarity conditions are established as follows:

$$\frac{C_\sigma}{C_\varepsilon C_E} = 1 \qquad (3)$$

where E represents the elastic modulus, $C_E = E_P/E_M$ is the elastic modulus similarity ratio;

In addition, the geo-mechanical model test requires the similarity ratio of all dimensionless physical

quantities (e.g., strain, internal friction angle, Poisson's ratio, etc.) to be 1. The similarity ratio of the same dimension physical quantity is equal, i.e.

$$C_\varepsilon = C_\phi = C_v = 1 \tag{4}$$

$$C_\sigma = C_E = C_c \tag{5}$$

where ϕ is the internal friction angle, v is the Poisson's ration, c is the cohesion. $C_\phi = \phi_P/\phi_M$ is the internal friction angle similarity ratio, $C_v = v_P/v_M$ is the Poisson's ratio similarity ratio, $C_c = c_P/c_M$ is the cohesion similarity ratio.

According to the dimensions of the main powerhouse and the size of the model test device (0.7 m × 0.7 m × 0.7 m), the geometric similarity ratio of the model test is determined to be $C_L = 300$. The unit weight similarity ratio is $C\gamma = 1$. So, the actual simulation range is 210 m × 210 m × 210 m.

3.2 Development of the Analogue Materials

3.2.1 Analogue Materials of Surrounding Rock

The iron-barites-silica cementation material (IBSCM), which was developed by Zhang et al. (2008) is selected to simulate the surrounding rock. The aggregates of IBSCM include iron ore powder, barite powder, and quartz sand. The cementing agent is rosin alcohol solution. The mechanical parameters of the analogue material can be adjusted by changing the content of each component and the concentration of cementitious agent. The physical and mechanical parameters of the protolith are shown in Table 1. According to the Eq. (1), the stress similarity scale is 300. Through large numbers of mechanical tests, such as uniaxial compression test, triaxial compression test and Brazilian test, the components proportion for analogue materials of surrounding rock is determined, as listed in Table 2. The physical and mechanical

parameters of the final analogue materials are shown in Table 1.

3.2.2 Analogue Material of Bolt and Cable

In the second model test, we use ABS (Acrylonitrile Butadiene Styrene plastic) material to simulate the fully bonded bolt and pre-stressed anchor cable. The prototype support scheme is shown in Fig. 1a. Since the layout and diameter of the bolt and cable are hard to be directly simulated by the geometric similarity scale, the equivalent of the bolt and cable was obtained through Zhu's method (Zhu et al. 2010, 2011). Due to the limitation of the model carven size, we adopted the support scheme as shown in Fig. 1b. Since the geometric similarity ratio is 300, the length of 80 mm in the model is equivalent to the actual length of 24,000 mm, that is, 1 support section in the model is equivalent to 6 support sections in the prototype In the prototype scheme, there are 28 pre-stressed anchor cables in one section, and the axial spacing of each section is 4000 mm. In the model scheme, there are 10 pre-stressed anchor cables in one section, and the axial spacing of each section is 80 mm. Therefore, 1 pre-stressed anchor cable in the model is approximately equivalent to 17 pre-stressed anchor cables in the prototype. In the same way, 1 rock bolt in the model is equivalent to 24 rock bolts in the prototype. The schematic illustration of the equivalence between the supporting plan of the prototype and the model is shown in Fig. 2.

The diameter of rock bolt and pre-stressed anchor cable in the model is determined through equivalent axial stiffness principle (Li et al. 2011).

$$C_K = \frac{E_P A_P/L_P}{E_M A_M/L_M} = \frac{C_E C_L^2}{C_L} = C_E C_L = 90,000 \tag{6}$$

Table 1 The physical and mechanical properties of the protolith and the analogous material

Material type	Unit weight (KN m^{-3})	Elastic modulus (MPa)	Uniaxial compressive strength (MPa)	Cohesion (MPa)	Internal friction angle (°)	Poisson's ratio
Protolith	26.6	41,500	128.8	22.5	54.2	0.27
Analogue material	26.2–26.8	135.1–142.9	0.419–0.457	0.72–0.77	51.6–56.1	0.26–0.28

Table 2 Components ratio of the analogue material

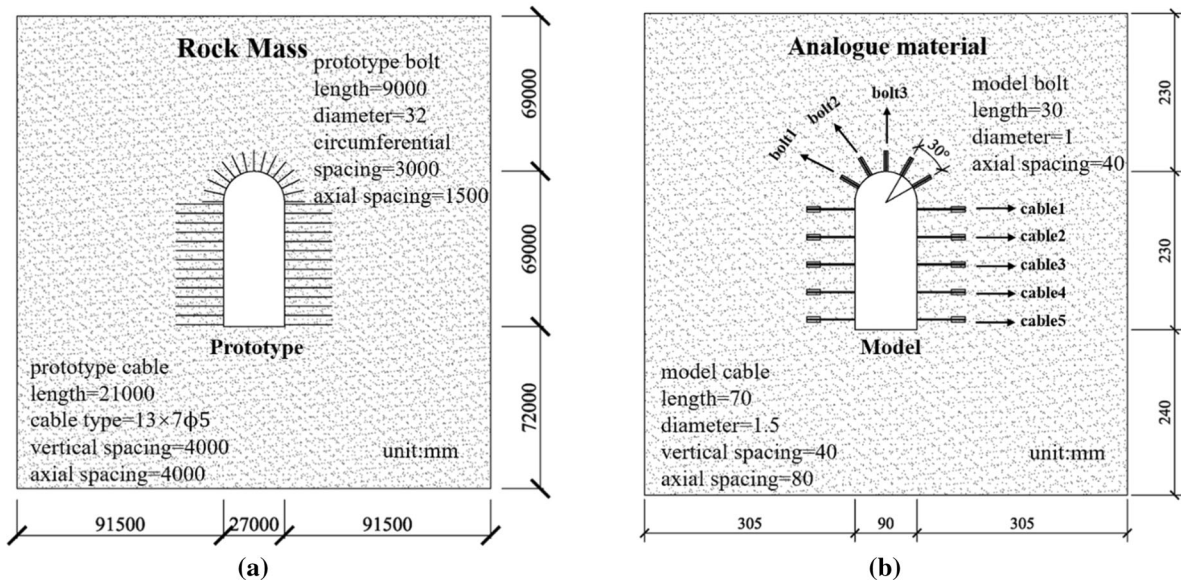| Iron powder:barite powder:silica sand	Cementing agent concentration (%)	Cementing agent as a percentage of aggregate weight (%)
1:1:0.5	6	5.5

Fig. 1 Dimensions of the prototype and the physical model of the hydropower house consisting of the support system. **a** The prototype; **b** the physical model

$$R_M = \sqrt{\frac{nE_P R_P^2 L_M}{E_M L_P C_K}} \qquad (7)$$

$$C_F = \frac{F_P}{F_M} = \frac{\sigma_P A_P}{\sigma_M A_M} = C_\sigma C_L^2 = 300^3 \qquad (8)$$

$$T_M = \frac{T_P n}{C_F} \qquad (9)$$

where C_K and C_F are the axial stiffness similarity ratio and the load similarity ratio; E denotes the elastic modulus, A denotes the cross-sectional area of the bolt or cable, L denotes the length, R denotes the diameter of the bolt or cable, F denotes the load, T denotes the prestress of the cable, n denotes the equivalent number of model bolt and model cable; subscript P and subscript M represent prototype and model, respectively.

The similarity ratio of axial stiffness is 90,000 according to Eq. (6). The diameter of the model rock bolt and pre-stressed anchor cable can be obtained from Eq. (7). For the pre-stress anchor cable, the magnitude of prestress is 1.26 N according to Eqs. (8) and (9). Table 3 presents the geometric and mechanical parameters of prototype and model rock bolts and pre-stressed anchor cable.

3.2.3 Analogue Material of Grout in the Cable Anchorage Section

The grout in the cable anchorage section is simulated by the mixture of barite powder, gypsum powder, glycerin and water. We take the elastic modulus, uniaxial compressive strength and tensile strength as the main parameters to simulate the prototype gout. Through a large number of mechanical tests on the analogue materials of different proportions, the mass ratio of barite powder, gypsum powder, glycerin and water is determined to be 9:1:0.2:9. Table 4 presents
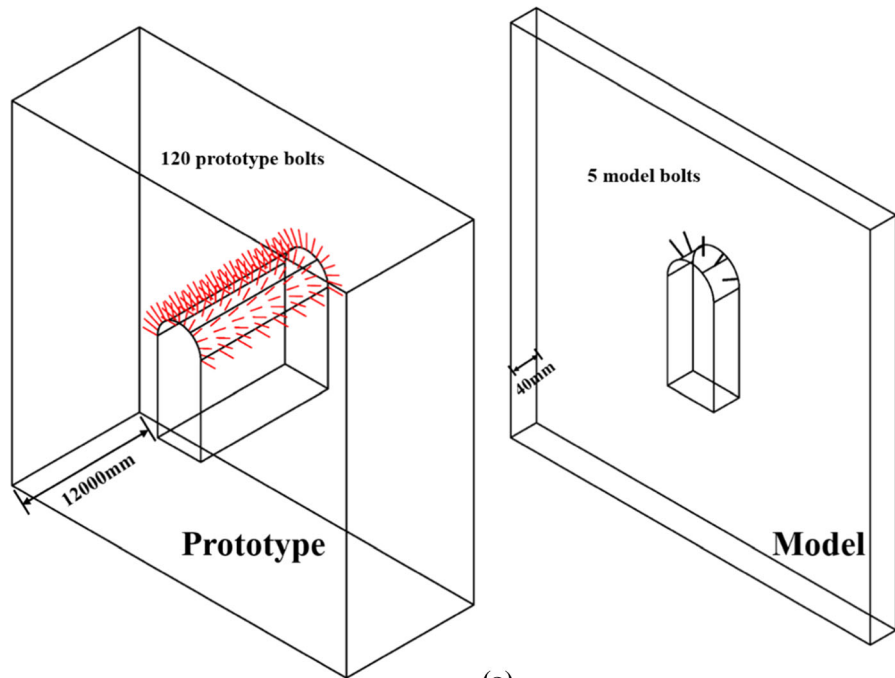
(a)
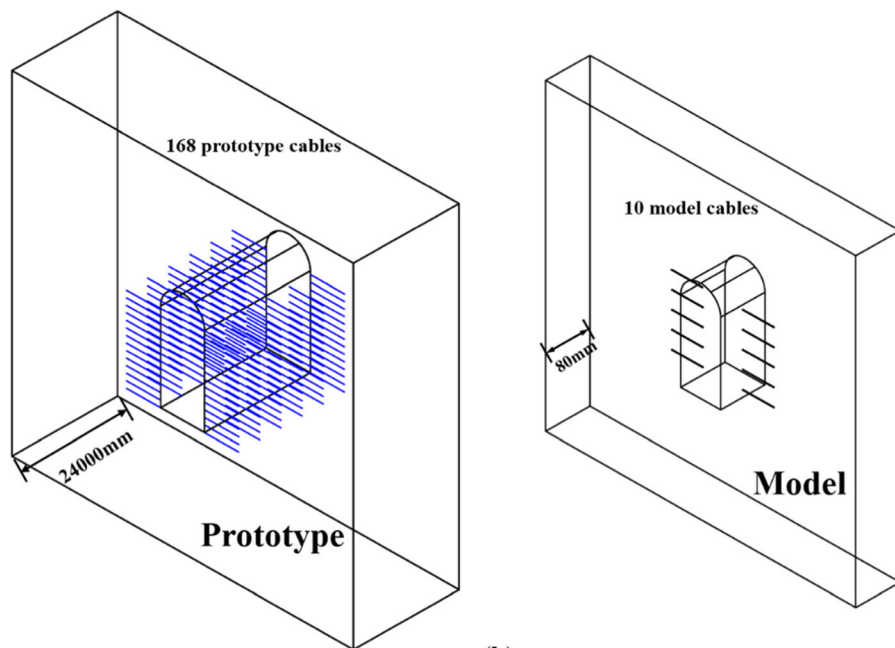
(b)

Fig. 2 Schematic illustration of support plan equivalence between prototype and model. **a** Schematic illustration of equivalence between the bolts in the prototype and the model;

b schematic illustration of equivalence between the cables in the prototype and the model

Table 3 Geometric and mechanical parameters of the anchorage support in prototype and the physical model

Category	Elastic modulus (MPa)	Diameter (mm)	Length (mm)	Axial spacing (mm)	Tensile strength (MPa)	Prestress (N)
Bolt in prototype	210,000	32	9000	1500	335	–
Bolt in model	200	1	30	40	4.5–4.8	–
Cable in prototype	195,000	47.7	21,000	4000	1670	2,000,000
Cable in model	200	1.5	70	80	4.5–4.8	1.26

Table 4 Comparison of mechanical parameters of cable anchorage section grout materials

Category	Elastic modulus (MPa)	Uniaxial compressive strength (MPa)	Tensile strength (MPa)
Prototype	32,000	36	3.3
Model	105–108	0.11–0.15	0.010–0.016

the comparison of the mechanical parameters between the model grout and the prototype grout.

3.3 Construction of the Model

The whole physical model is built by statically compacting materials layer by layer. The whole model is constructed by 10 layers with the thickness of each layer to be 70 mm. The general procedure of building physical model is shown in Fig. 3a–d. The construction procedure of the model is as follows: (1) Fill in the material and compact the material preliminarily. (2) Embed the measuring components at the designed positions (Fig. 8a) including optical multipoint displacement meter and miniature pressure cell. And embed the support components at the designed position (Fig. 1b) in the model test 2. (3) Compact the material. (4) Air drying and maintenance. (5) Repeat procedure (1)–(4) until the model construction is finished.

The whole model test system is shown in Fig. 4. It is mainly composed of the counter-force frame system with the overall size of 1.75 m × 1.75 m × 2.0 m (width × height × depth), the intelligent hydraulic 3D loading system, and the automatic data acquisition system. The installation of rock bolts and pre-stressed anchor cable adopts the pre-embedded method in the second model test. Figure 5 shows the embedding method of pre-stressed anchor cable.

1. place the cable in the excavated groove.
2. compress the free anchor plate 3 to the fixed anchor plate 4 with the hard sheet 2, which makes length of the section I (see Fig. 5) reach nearly 0. The spring between the two plates is customized spring. When the spring is fully compressed, its elastic force will reach about 1.26 N.
3. fill analogue material into the section II (see Fig. 5) and compact the material preliminarily.
4. pull out the hard sheet and fill the section I with analogue material.

When the cavern is excavated, section I will be exposed to the air and the spring will rebound, which makes the prestress applied to the anchor cable (Fig. 6). In order to demonstrate the process of applying prestress, the length of the spring in Fig. 6 is deliberately enlarged. In actual situation, the length of the L section is still very small after excavation.

3.4 Lay Out of the Measuring Points

As shown in Fig. 7, four monitoring sections are set. Section I is the monitoring section of rock bolts and pre-stressed anchor cable with a thickness of 40 mm. The layout of strain gauge is shown in Fig. 8b, c. The strain gauge of rock bolt is attached to the external surface of grouting, and the strain gauge of pre-stressed anchor cable is attached to the external surface of cable rod. Section II is radial stress
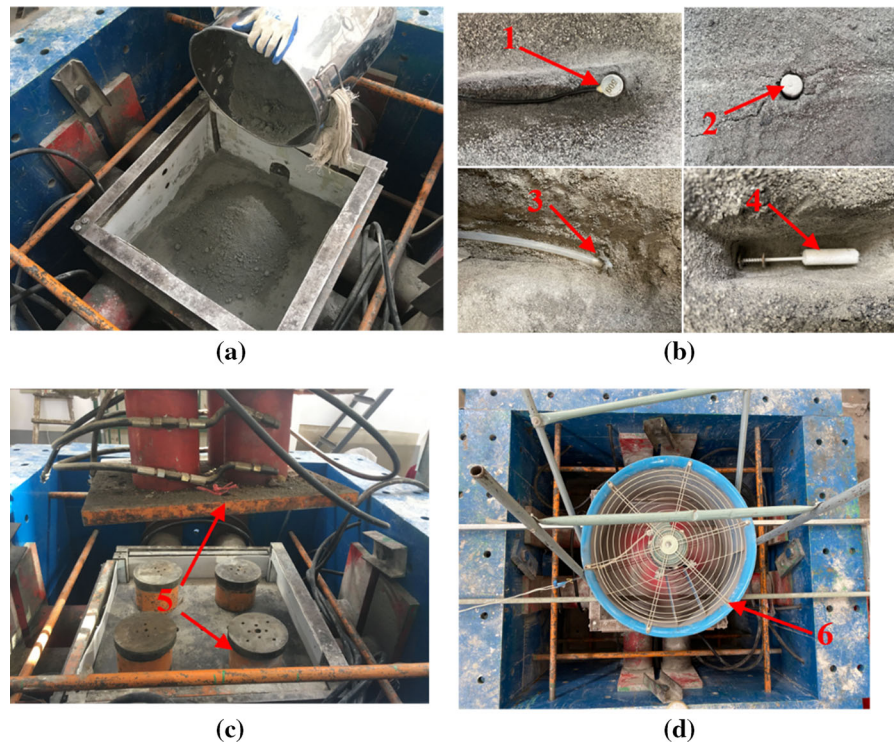
Fig. 3 The general procedure of physical model construction. **a** Paving analogue materials; **b** embedding test sensors and support components; **c** compacting analogue materials; **d** air

drying; 1—miniature pressure cell; 2—model bolt; 3—miniature multipoint displacement meter; 4—model cable; 5—compaction apparatus; 6—air dryer
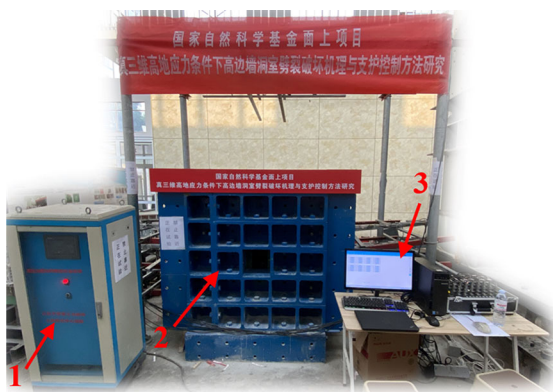

Fig. 4 Overview of the geo-mechanical model test system. 1—Intelligent hydraulic 3D loading system; 2—Counter-force frame system; 3—Automatic data acquisition system

monitoring section. Section III is displacement monitoring section and Section IV is tangential stress monitoring section. The same layout is used for optical multipoint displacement meter and miniature pressure cell, which is shown in Fig. 8a.

3.5 Model Excavation

After the construction of the model, the boundary load is applied by the self-developed true three-dimensional loading system to form the initial ground stress field similar to the prototype, as shown in Fig. 9. The six surfaces of the model are loaded step by step according to the proportion until the designed value is reached. After that, the load is kept stable for at least 24 h before the excavation of the cavern.

The excavation of the underground powerhouse is conducted by manual drilling and excavation. Three excavation layers are designed from top to bottom. The next layer is excavated after the completion of the upper one, as shown in Fig. 10. Each layer is excavated in 17 steps, with the excavation footage of each step equals to 40 mm (equivalent to 12 m of the prototype). The excavation is suspended after each step of excavation. The readings of each measuring instrument are recorded after the data is stable. Then the next step of excavation is carried out until the excavation of the cavern is completed. During the
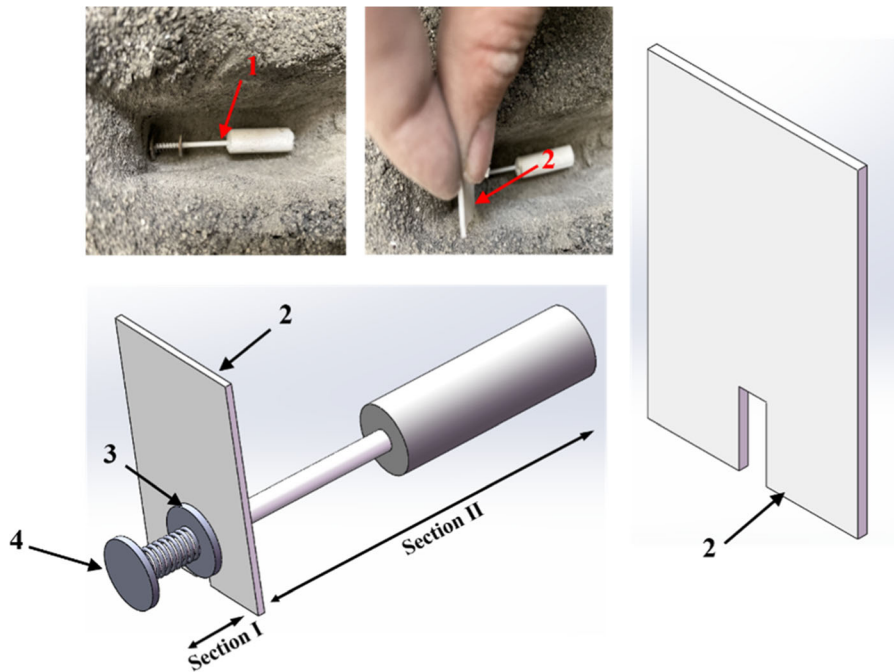
Fig. 5 Schematic diagram of the embedded cable. 1—Model cable; 2—hard sheet with a notch underneath; 3—free anchor plate; 4–fixed anchor plate
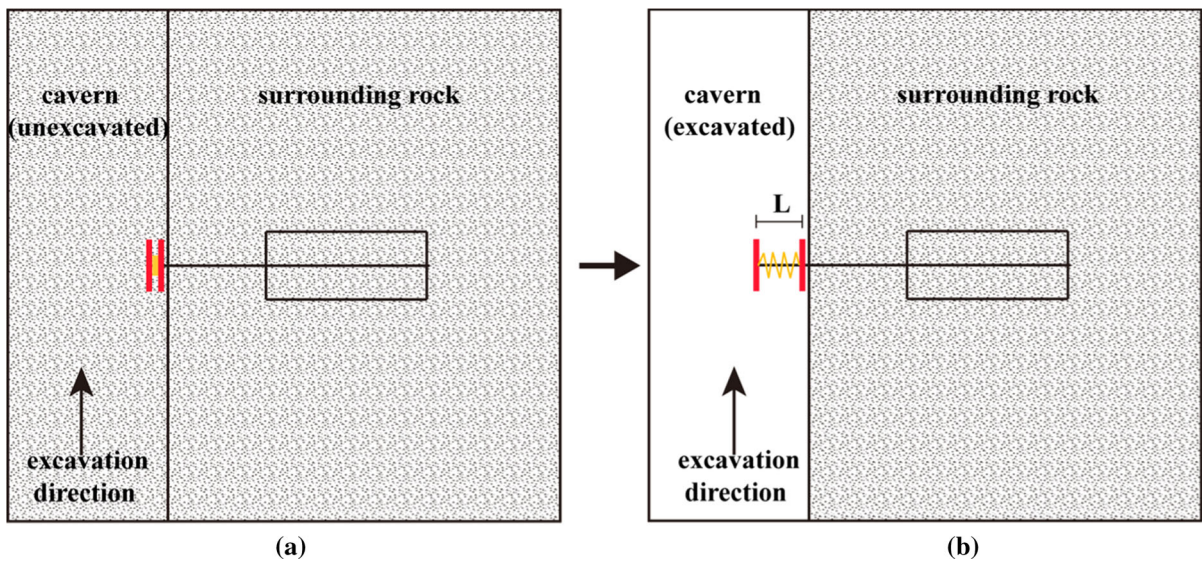

Fig. 6 Schematic diagram of prestress application. **a** An embedded cable before excavation; **b** an embedded cable after excavation

model excavation, the high-speed static resistance strain gauge measurement system and grating scale multi-point displacement gauge measurement system are used to monitor the stress, displacement in surrounding rock and the change of the strain of anchor bolt and anchor cable.
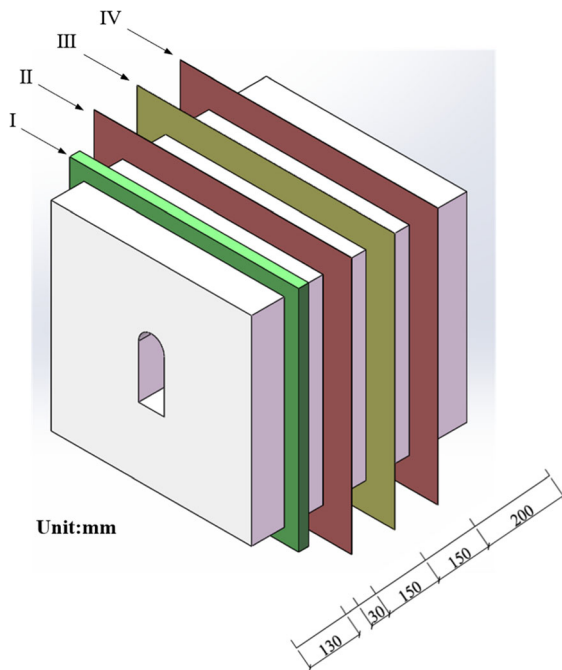
Fig. 7 Layout of the monitoring sections. Section I: The axial force of bolts and cables monitoring section; Section II: The radial stress monitoring section; Section III: The radial displacement monitoring section; Section IV: The tangential stress monitoring section

4 Results and Discussion

In the following part, the displacement and stress obtained from the model test are converted into the prototype following the similarity criterion. Theoretically, the distribution of stress and displacement on the left and right sides of the cavern are symmetric. Thus, the results of the right-side wall, right haunch and vault are presented and analyzed. After the model test, the front part of the model is cut to check the failure patterns of the surrounding rock. Figure 11 displays the photos of dissembled model which show the fracture patterns of the surrounding rock after the excavation.

4.1 Displacement

Figure 12a shows the evolution of radial displacement at right-side wall, right haunch and vault with excavation step in the second model test. Figure 12b

shows the distribution of radial displacement of surrounding rock around the cavern after excavation.

From Fig. 12, it can be concluded that:

In the second model test, the deformation is toward the inside of the cavern. The displacement around the cavern increases with the excavation footage. Before the tunnel face reaches the monitoring section, the displacement increases significantly. After the excavation, the displacement at the side wall is the largest, which is about 2 times of the settlement of the vault. The reason for this phenomenon is that the cavern is large, and there are no constraints (such as surrounding rocks) near the middle of the sidewall to limit its horizontal deformation. When the tunnel face exceeds the monitoring section, the displacement at the monitoring section still increases substantially to a certain extent. The maximum increment occurs at the side wall, with a magnitude of 6 mm.

The excavation time to the monitoring section is marked by a dashed line in Fig. 12a. the displacements before and after excavation indicate that: during the excavation of the first and second layers, the deformation of the surrounding rock in front of and behind the tunnel face is obviously affected by the excavation disturbance. the influence range is about 1.0R (R is the cavern span). In the excavation of the third layers, along the cavern axis, the influence range of the excavation disturbance is about 1.5R ahead and behind the tunnel face. Due to the rock bolt and pre-stressed anchor cable support, the influence of excavation on vault and haunch is not significant, and the displacement rarely increases.

In the unsupported model, the displacement presents the undulate changing status, wherein the wave crest and the trough are arranged alternately. In the anchored model, the displacement around the cavern decreases monotonously with increasing distance from tunnel periphery along the radial direction of the cavern. The maximum displacement is located at the side wall. The range of excavation disturbance zone at the side wall is 2.0R along the radial direction of the cavern, beyond which the influence of the excavation disturbance on the deformation of the surrounding rock is very minor. Table 5 compares the radial displacements measured from the model test under support and without support at key locations around the cavern. On the whole, the displacement
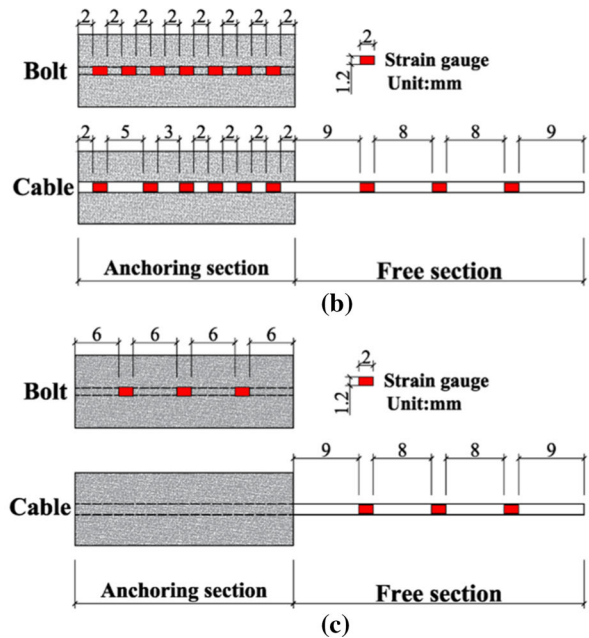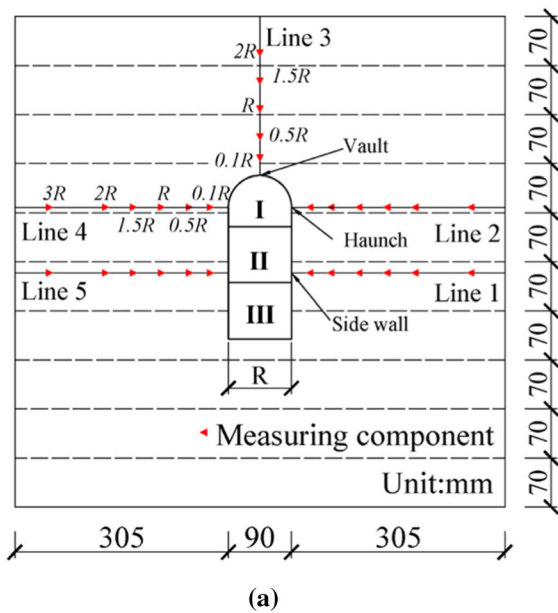
(a)

(b)

(c)

Fig. 8 Layout of the monitoring points. **a** Layout of displacement and stress monitoring points; **b** measuring points on bolt3 and cable3 (bolt3 and cable3 can be seen in Fig. 1); **c** measuring points on bolt1, bolt2, cable1, cable2, cable4, and cable5 (bolt1, bolt2 and cable1, cable2, cable4, cable5 can be seen in Fig. 1). I—First excavation layer; II–Second excavation layer; III—Third excavation layer
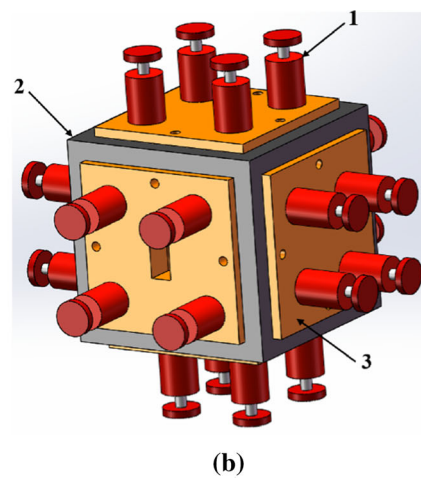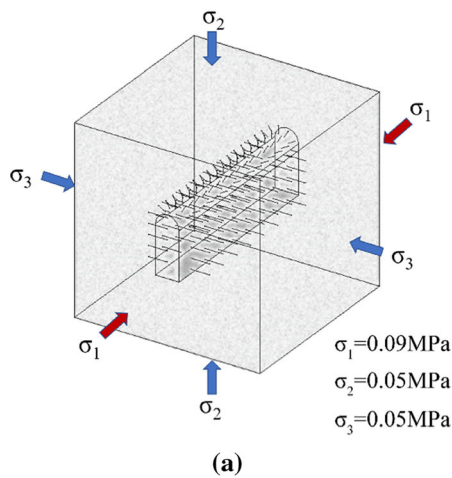

(a)

(b)

Fig. 9 **a** Loading scheme of the geo-mechanical model; **b** schematic diagram of the 3D hydraulic loading system. 1—Hydraulic cylinder; 2—Guide frame; 3—Force transmitter

after support is at least 64% less than that without support, and the distribution of displacement is improved. Therefore, the surrounding rock is in a safe and stable state, without the trend of splitting failure, indicating that the rock bolt and prestressed anchor cable support notably improves the overall stability of surrounding rock in the anchorage area.

4.2 Stress in the Surrounding Rock

Figure 13a, b present the variations of the radial stress and tangential stress in the surrounding rock versus the excavation step. Figure 13c, d show the distributions of radial stress and tangential stress in the surrounding rock after the excavation. Table 6 presents the
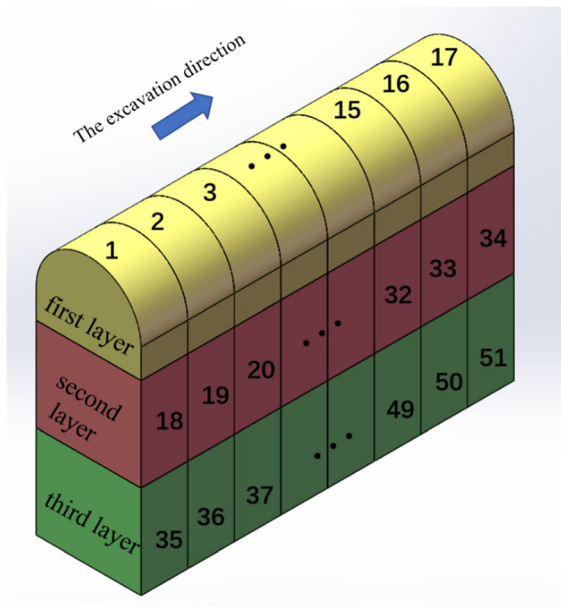
Fig. 10 The procedure of cavern excavation

comparison between the stresses in surrounding rock measured from the anchored model test and the model test without anchoring at key locations around the cavern.

From Fig. 13, it can be seen that:

As a result of the excavation-induced unloading, the radial stress in surrounding rock is released. The radial stress of the haunch is released for the first time when the first layer is excavated to the monitoring section. The radial stress decreases slightly when the second layer is excavated to the monitoring section, and the final radial stress is released by 76%. It is worth noting that there is a small short-term stress

concentration before the radial stress release at the vault and the haunch. This phenomenon can be attributed to the fact that the surrounding rock in front of the tunnel face extrudes to the free face as a result of excavation. It is particularly obvious in the hard rock tunnel. However, in the latter two layers of excavation, this phenomenon is not obvious, because the area of the tunnel face is larger, and the cross-section shape is less circular, weakening the constraint effect of the tunnel face. The radial stress at the side wall is released twice, by 79% for the first time and by 9.5% for the second time based on the original rock stress. The tangential stress increases due to the excavation-induced unloading. When the second layer is excavated to the monitoring section, the tangential stress at the haunch decreases, which is still greater than the original rock stress. At the same time, the tangential stress concentrates at the side wall, which indicates that the concentration area of tangential stress has moved towards the bottom of the cavern. When the third layer is excavated to the monitoring section, the tangential stress at the side wall decreases greatly.

In the supported model test, the distribution of the radial stress along the radial direction follows the same rule, that is, the closer to the cavern periphery, the smaller the radial stress. With the increase of the distance from the cavern periphery, the radial stress gradually returns to the original in-situ stress. The distribution of the tangential stress in the vault and haunch is opposite to the radial stress, and the maximum tangential stress exists near the cavern periphery. The tangential stress at the side wall increases first and then decreases with the distance from the cavern periphery, which presents the same
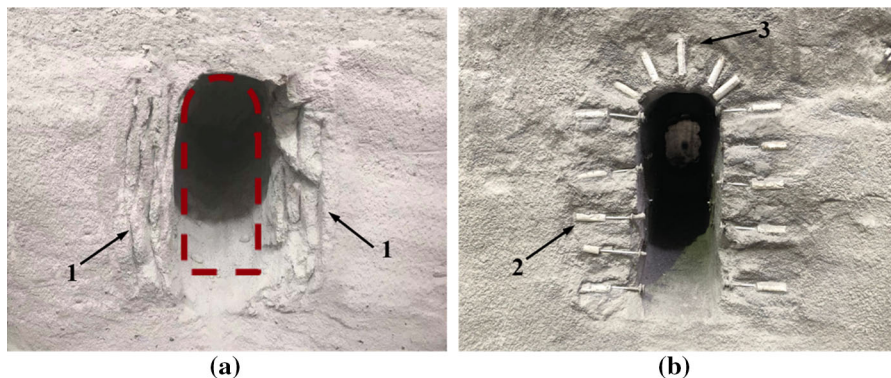

Fig. 11 Photos of the middle section of the cavern after excavation. **a** The non-anchoring model; **b** the anchored model. 1—Fractured zone; 2–pre-stressed anchor cable; 3—rockbolt
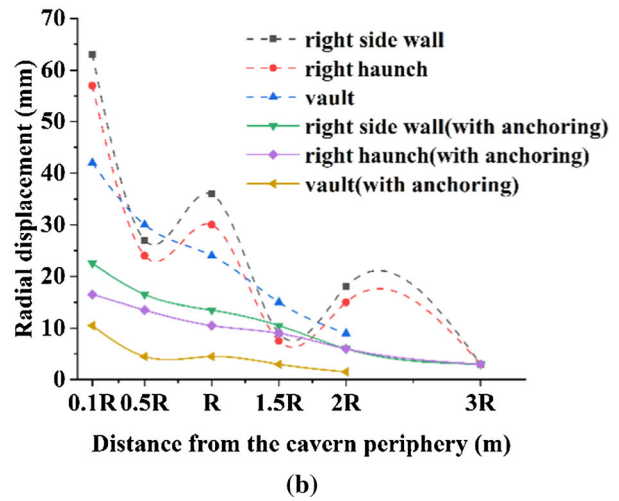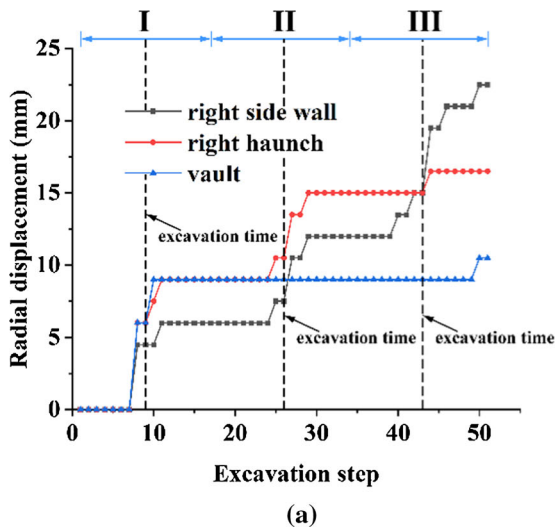
Fig. 12 a Radial displacement of the right side wall, the right haunch and the vault of the cavern versus the excavation step in second model test; b distribution of radial displacement in surrounding rock around the cavern after the excavation. R is the span of the cavern. I—First excavation layer; II—Second excavation layer; III—Third excavation layer

Table 5 Comparison between the radial displacements of surrounding rock measured from the anchored model test and the model test without anchoring at key locations around the cavern

Type	Side wall (mm)	Haunch (mm)	Vault (mm)
Model test (with anchoring)	22.5	16.5	10.5
Model test (without anchoring)	63.0	57.0	42.0

varying trend as the unsupported model within 1.5R. Compared with the unsupported model, the radial stress with support is larger. The tangential stress of the supported model is larger within the range of R, and smaller outside R (including R). It shows that bolt and cable support strengthens the surrounding rock, improves the overall stability and stress distribution of the surrounding rock.

4.3 Axial Force on the Bolts and Cables

In this study, it is assumed that rock bolts and pre-stressed anchor cables stay in the elastic state. The axial force can be calculated according to the linear elastic relationship. Because the diameter of the bolt is too small, the bolt and grout are regarded as the composite rod to measure the axial strain, and the axial force of the composite rod and the shear stress of the grout interface are obtained by Eqs. 10 and 11. The equivalent elastic modulus and the equivalent cross-sectional area of the composite rod are calculated by Eqs. 12 and 13. The axial force of pre-stressed anchor cable is obtained by Eq. 10.

$$F_i = E\varepsilon_i A \tag{10}$$

$$\tau_i = \frac{F_{i+1} - F_i}{\pi R l_i} \tag{11}$$

$$E_c = \frac{E_g A_g + E_a A_a}{A_g + A_a} \tag{12}$$

$$A = A_g + A_a \tag{13}$$

where F_i is the axial force of the rock bolt or pre-stressed anchor cable, ε_i is the monitored axial strain at the i th strain gauge, E is the elastic modulus of the composite rod or pre-stressed anchor cable and A is the cross-sectional area of the composite rod or pre-stressed anchor cable. τ_i is the interface shear stress on the grout surface, F_{i+1} and F_i are the rock bolt axial force at two adjacent strain gauge, R is the diameter of the composite rod, l_i is the distance of two adjacent strain gauge. E_g and E_a are the elastic modulus of the grout and bolt, A_g and A_a are the cross-sectional area of the grout and bolt.
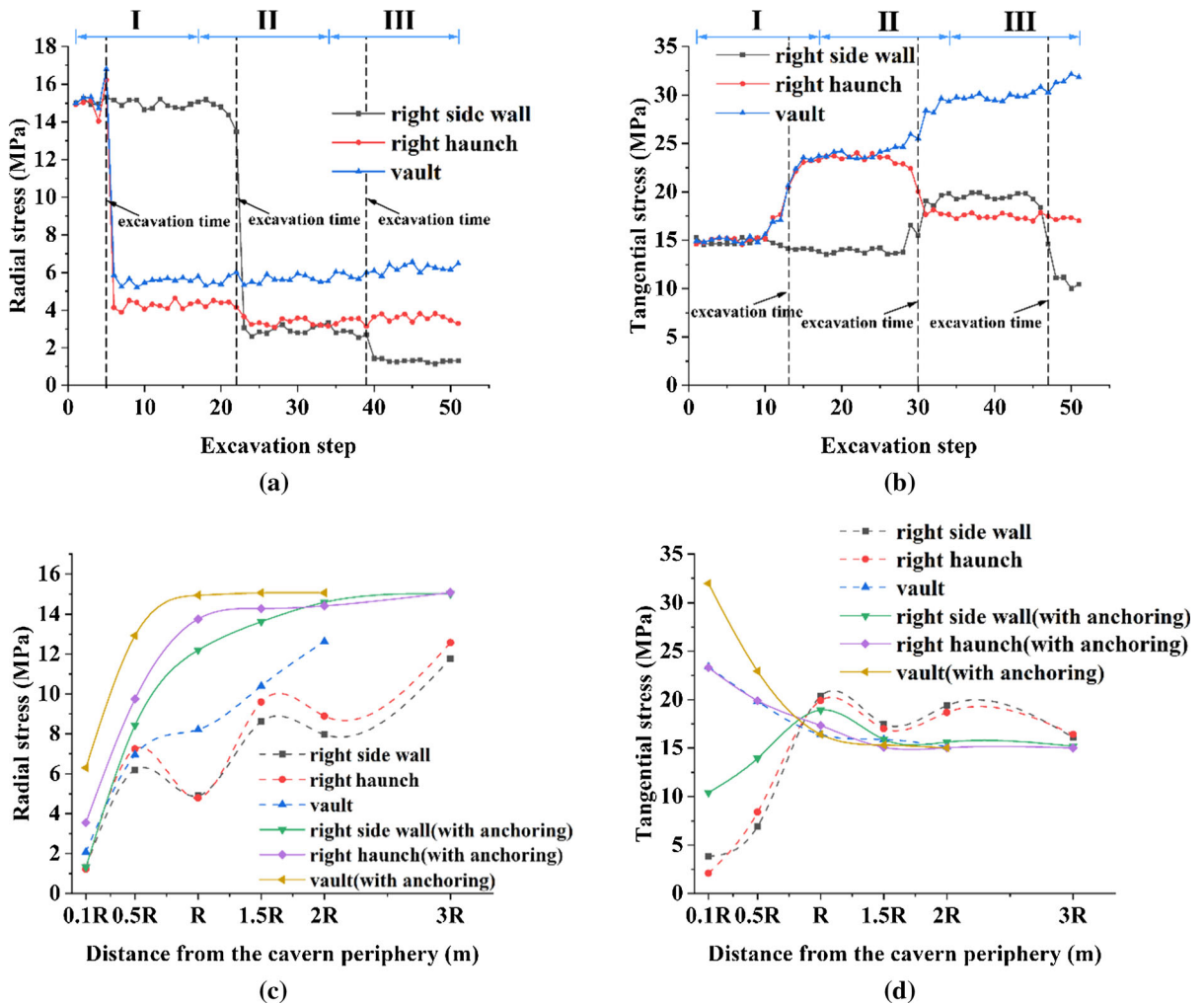
(a)

(b)

(c)

(d)

Fig. 13 a Radial stresses in the surrounding rock versus the excavation step in second model test; **b** tangential stresses in the surrounding rock versus the excavation step in second model test; **c** radial stresses in surrounding rock after the excavation;

d Tangential stresses in surrounding rock after the excavation. I—First excavation layer; II—Second excavation layer; III–Third excavation layer; R is the span of the cavern

Table 6 Comparison between the stresses in surrounding rock measured from the anchored model test and the model test without anchoring at key locations around the cavern

Type	Side wall σ_r (MPa)	Side wall σ_t (MPa)	Haunch σ_r (MPa)	Haunch σ_t (MPa)	Vault σ_r (MPa)	Vault σ_t (MPa)
Model test (with anchoring)	1.3	10.4	3.6	17.4	6.3	32.3
Model test (without anchoring)	1.3	3.8	1.2	2.1	2.1	23.4

σ_r and σ_t are the radial stress and the tangential stress

Variation of the axial force on the rock bolt and pre-stressed anchor cable with excavation step is shown in Fig. 14a, b. The distributions of axial force and shear force along the bolt are presented in Fig. 14c, and the distribution of axial force along the cable is shown in Fig. 14d.

During the whole excavation process, three steps of growth can be noted from the axial force of the rock bolt, corresponding to the steps when excavation reaches the monitoring section. The increasing rate of rock bolt axial force decreases until the force reaches a stable state in the last few steps of excavation. The axial force of all bolts is positive during excavation.

The phenomenon that tension and compression alternate in the bolt does not occur (Chen et al. 2013; Zhu et al. 2019), indicating that there is no break tendency at vault and haunch. The prestressing force is applied when the free anchor plate 3 and fixed anchor plate 4 (see Fig. 5) are exposed to the air during the excavation. The axial force of the anchor cable fluctuates slightly and stabilizes gradually as the excavation progresses. The axial force of cable 1 increases by 13% during the excavation of the second layer. Then during the excavation of the third layer, the prestress of the remaining anchor cable can be applied. The overall support is formed, and the axial force of cable 1
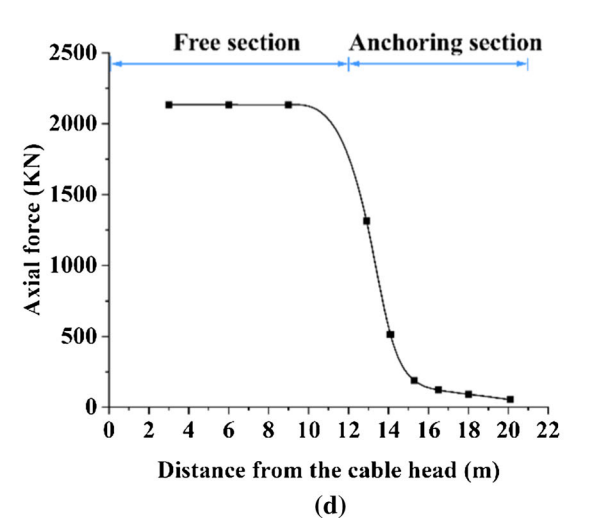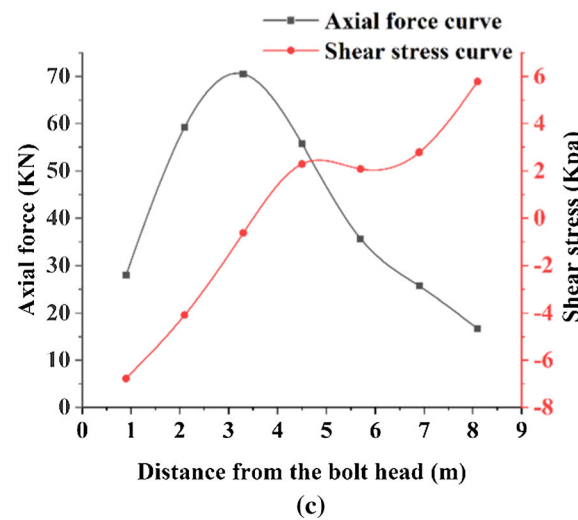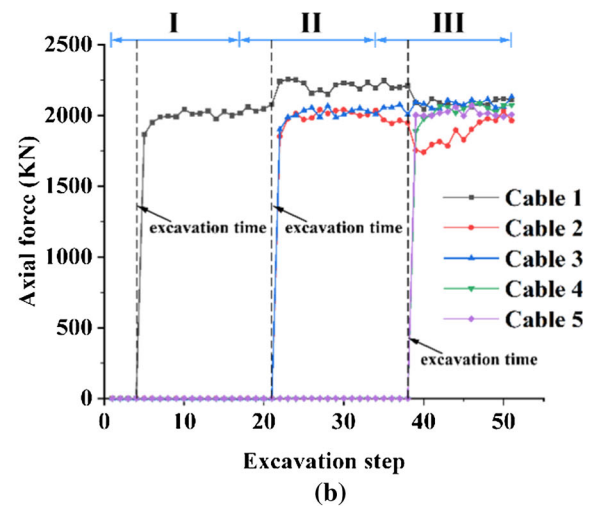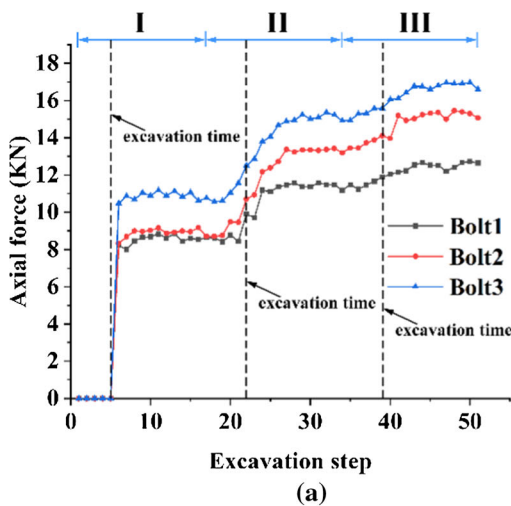

Fig. 14 **a** Axial force of rockbolt versus excavation step; **b** axial force of pre-stressed anchor cable versus excavation step; **c** axial force and shear stress along the bolt3 after the excavation; **d** axial force along the cable3 after the excavation (bolt 3 and cable 3 can be seen in Fig. 1). I—First excavation layer; II—Second excavation layer; III—Third excavation layer

and 2 is reduced. As the deformation of surrounding rock continues to increase, the axial forces of cable 1 and 2 increase slightly.

The axial force on the bolt is tensile force. The distribution along the bolt is "small at both ends and large in the middle". The magnitude of the shear stress on the interface increases gradually from the middle section to the ends. The shear stress reaches 0 at the position where the axial force is maximum, that is, about 3.3 m away from the bolt head. Freeman (Freeman et al. 1978) calls this point "neutral point". The part of the bolt that starts from the neutral point and points to the cavern is called "pick up part", and the part of the bolt that starts from the neutral point and points to the deep surrounding rock is called "anchor part". In this test, the length of pick up part is about 2 m, and the length of anchor part is about 5 m. The positive shear stress on the "anchor part" restrains the movement of the bolt into the cavern, while the negative shear stress on the "pick up part" ensures the balance of the bolt. The axial force of the pre-stressed anchor cable free section remains basically the same, about 2100KN. In the anchoring section of the cable, the axial force reaches the maximum at the beginning, and attenuates towards the deep surrounding rock direction, and the attenuation amplitude decreases with the increase of depth. The axial force of the anchoring section is mainly concentrated in the first 5 m, which indicates that only the first 5 m of the anchoring section plays an anchoring role.

5 Conclusions

Based on the Pubugou Hydropower Station, we have conducted two true three-dimensional geomechanical model tests to reveal the support control of the splitting failure in the cavern with high side wall. The following conclusions are obtained.

1. Splitting failure occurs at the side wall in the unsupported model, while no splitting failure occurs in the supported model, indicating that the anchorage support can inhibit the occurrence of splitting failure.
2. In the unsupported model, the stress and displacement at the side wall and haunch show non-monotonic changes with alternating peaks and troughs, while the displacement and radial stress present monotonic variation in the supported model.
3. In the supported model, the maximum displacement appears at the side wall of the cavern. The stress concentration area at the side wall has moved towards the bottom of the cavern in the process of layered excavation.
4. In the supported model, the radial stress is larger than that without support, and the tangential stress is larger within the range of span of the cavern (R) from the cavern periphery, yet smaller outside this range. The tangential stress at the side wall shows the same varying trend as the unsupported model within 1.5R from the cavern periphery, that is, it first increases and then decreases with the distance from the cavern periphery.
5. The axial force of bolts is positive. With the progress of excavation, axial force increases continuously, but the increase amplitude decreases gradually. The axial force in the anchoring section of the cable decreases sharply and mainly concentrates in the first 5 m, which indicates that only the first 5 m of the anchoring section plays an anchoring role.

The anchor support restrains the occurrence of splitting failure, so the optimization of parameters of rock bolt and pre-stressed anchor cable are of great significance to the stability of deep buried high side wall cavern.

Declarations

Conflict of interest The authors declared that they have no conflict of interest to this work.

References

Behnia M, Seifabad MC (2018) Stability analysis and optimization of the support system of an underground powerhouse cavern considering rock mass variability. Environ Earth Sci. https://doi.org/10.1007/s12665-018-7835-2

Boon CW, Houlsby GT, Utili S (2015) Designing tunnel support in jointed rock masses via the DEM. Rock Mech Rock Eng 48(2):603–632. https://doi.org/10.1007/s00603-014-0579-8

Chen X, Zhang Q, Wang Y, Liu D, Zhang N (2013) Model test of anchoring effect on zonal disintegration in deep surrounding rock masses. Sci World J 2013:1–16. https://doi.org/10.1155/2013/935148

Chen XG, Zhang N, Ma TC, Niu XD, Liu XX, Feng T (2018) Energy-based forming and anchoring mechanism and criterion for zonal disintegration. Theoret Appl Fract Mech 97:349–356. https://doi.org/10.1016/j.tafmec.2017.06.006

Du K, Tao M, Li XB, Zhou J (2016) Experimental study of slabbing and rockburst induced by true-triaxial unloading and local dynamic disturbance. Rock Mech Rock Eng 49(9):3437–3453. https://doi.org/10.1007/s00603-016-0990-4

Fahimifar A, Soroush H (2005) A theoretical approach for analysis of the interaction between grouted rockbolts and rock masses. Tunn Undergr Space Technol 20(4):333–343. https://doi.org/10.1016/j.tust.2004.12.005

Freeman TJ (1978) The behavior of fully bonded rock bolts in the kielder experimental tunnel. Tunnels Tunn 10:37–40

Fumagalli E (1973) Statical and geomechanical models, statical and geomechanical models. Springer. https://doi.org/10.1007/978-3-7091-8317-5

Gao M, Liang ZZ, Jia SP, Li YC, Yang XX (2019) An equivalent anchoring method for anisotropic rock masses in underground tunnelling. Tunn Undergr Space Technol 85:294–306. https://doi.org/10.1016/j.tust.2018.12.017

Gong FQ, Wu WX, Li TB, Si XF (2019) Experimental simulation and investigation of spalling failure of rectangular tunnel under different three-dimensional stress states. Int J Rock Mech Min Sci. https://doi.org/10.1016/j.ijrmms.2019.104081

Guo Q, Li JT, Zhao YL (2010) Splitting failure criterion and numerical simulation for underground surrounding rock masses. Chin J Central South Univ 41:1535–1539

Hibino S (2001) Rock mass behavior of large-scale cavern during excavation and trend of underground space use. J Min Mater 117(3):167–175. https://doi.org/10.2473/shigentosozai.117.167

Hibino S, Motojima M (1995) Characteristic behavior of rock mass during excavation of large scale caverns. In 8th ISRM Congress. International Society for Rock Mechanics and Rock Engineering

Li SC, Liu Q, Li LP, Zhao Y, Wang HP, Zhao Y, Yuan XS (2011) Development of large-scale geomechanical model test system for tunnel construction and its application. Chin J Rock Mech Eng 30(07):1368–1374

Li Y, Zhu WS, Fu JW, Guo YH, Qi YP (2014) A damage rheology model applied to analysis of splitting failure in underground caverns of Jinping I hydropower station. Int J Rock Mech Min Sci 71:224–234. https://doi.org/10.1016/j.ijrmms.2014.04.027

Li XW, Nemcik J, Mirzaghorbanali A, Aziz N, Rasekh H (2015) Analytical model of shear behaviour of a fully grouted cable bolt subjected to shearing. Int J Rock Mech Min Sci 80:31–39. https://doi.org/10.1016/j.ijrmms.2015.09.005

Li Y, Zhou H, Zhang L, Zhu WS, Li SC, Liu J (2016) Experimental and numerical investigations on mechanical property and reinforcement effect of bolted jointed rock mass. Constr Build Mater 126:843–856. https://doi.org/10.1016/j.conbuildmat.2016.09.100

Li HB, Yang XG, Zhang XB, Zhou JW (2017) Deformation and failure analyses of large underground caverns during construction of the Houziyan Hydropower Station, Southwest China. Eng Fail Anal 80:164–185. https://doi.org/10.1016/j.engfailanal.2017.06.037

Liu GF, Feng XT, Jiang Q, Yao ZB, Li SJ (2017) In situ observation of spalling process of intact rock mass at large cavern excavation. Eng Geol 226:52–69. https://doi.org/10.1016/j.enggeo.2017.05.012

Liu J, Zhao XD, Zhang SJ, Xie LK (2018) Analysis of support requirements for underground water-sealed oil storage cavern in China. Tunn Undergr Space Technol 71:36–46. https://doi.org/10.1016/j.tust.2017.08.013

Luo Y, Gong FQ, Liu DQ, Wang SY, Si XF (2019) Experimental simulation analysis of the process and failure characteristics of spalling in D-shaped tunnels under true-triaxial loading conditions. Tunn Undergr Space Technol 90:42–61. https://doi.org/10.1016/j.tust.2019.04.020

Ma K, Feng B, Zhuang DY, Guo XF, Gao Q (2020) Distance effects of the fault on the surrounding rock mass stability of the main powerhouse at the Huanggou pumped-storage power station. Tunn Undergr Sp Technol. https://doi.org/10.1016/j.tust.2020.103568

Malmgren L, Nordlund E (2008) Interaction of shotcrete with rock and rock bolts—a numerical study. Int J Rock Mech Min Sci 45(4):538–553. https://doi.org/10.1016/j.ijrmms.2007.07.024

Prasad VVR, Dwivedi RD, Swarup A (2013) Determination of support pressure for tunnels and caverns using block theory. Tunn Undergr Space Technol 37:55–61. https://doi.org/10.1016/j.tust.2013.03.006

Qian QH, Zhou XP (2018) Failure behaviors and rock deformation during excavation of underground cavern group for Jinping I Hydropower Station. Rock Mech Rock Eng 51(8):2639–2651. https://doi.org/10.1007/s00603-018-1518-x

Shang J (2020) Rupture of veined granite in polyaxial compression: insights from three-dimensional discrete element method modeling. J Geophys Res Solid Earth. https://doi.org/10.1029/2019JB019052

Tang CA, Wong WHC, Chau KT, Lin P (2005) Modeling of compression-induced splitting failure in heterogeneous brittle porous solids. Eng Fract Mech 72(4):597–615. https://doi.org/10.1016/j.engfracmech.2004.04.008

Xiao XH, Xiao PW, Dai F, Li HB, Zhang XB, Zhou JW (2018) Large deformation characteristics and reinforcement measures for a rock pillar in the Houziyan Underground Powerhouse. Rock Mech Rock Eng 51(2):561–578. https://doi.org/10.1007/s00603-017-1329-5

Yoshida T, Ohnishi Y, Nishiyama S, Hirakawa Y, Mori S (2004) Behavior of discontinuties during excavation of two large underground caverns. Int J Rock Mech Min Sci Proc ISRM SINOROCK 2004 Symp 41:864–869

Zhang QY, Li SC, Guo XH, Li Y, Wang HP (2008) Research and development of new typed cementitious geotechnical similar material for iron crystal sand and its application. Chin J Rock Soil Mech 29(8):2126–2130

Zhang QY, Ren MY, Duan K, Wang WS, Gao Q, Lin HX, Xiang W, Jiao YY (2019a) Geo-mechanical model test on the collaborative bearing effect of rock-support system for

deep tunnel in complicated rock strata. Tunn Undergr Space Technol. https://doi.org/10.1016/j.tust.2019.103001

Zhang QY, Zhang Y, Duan K, Liu CC, Miao YS, Wu D (2019b) Large-scale geo-mechanical model tests for the stability assessment of deep underground complex under true-tri-axial stress. Tunn Undergr Space Technol 83:577–591. https://doi.org/10.1016/j.tust.2018.10.011

Zhang QY, Liu CC, Duan K, Zhang ZJ, Xiang W (2020) True three-dimensional geomechanical model tests for stability analysis of surrounding rock during the excavation of a deep underground laboratory. Rock Mech Rock Eng 53(2):517–537. https://doi.org/10.1007/s00603-019-01927-0

Zhou H, Xu RC, Lu JJ, Zhang CQ, Meng FZ, Sheng J (2015) Experimental investigations and mechanism analysis of anchoring effect of pre-stressed bolts for slabbing sur-rounding rock in deep tunnel. Chin J Rock Mech Eng 34(06):1081–1090. https://doi.org/10.13722/j.cnki.jrme.2014.0726

Zhu WS, Zhang QB, Zhu HH, Li Y, Yin JH, Li SC, Sun LF, Zhang L (2010) Large-scale geomechanical model testing of an underground cavern group in a true three-dimensional (3-D) stress state. Can Geotech J 47(9):935–946. https://doi.org/10.1139/T10-006

Zhu WS, Li Y, Li SC, Wang SG, Zhang QB (2011) Quasi-three-dimensional physical model tests on a cavern complex under high in-situ stresses. Int J Rock Mech Min Sci 48(2):199–209. https://doi.org/10.1016/j.ijrmms.2010.11.008

Zhu WS, Yang WM, Li XJ, Xiang L, Yu DJ (2014) Study on splitting failure in rock masses by simulation test, site monitoring and energy model. Tunn Undergr Space Technol 41:152–164. https://doi.org/10.1016/j.tust.2013.12.007

Zhu XG, Chen ZL, Ren Y (2019) Numerical simulation study on the anchorage mechanism of yield supporting in deep tunnel. Geotech Geol Eng 37(3):2091–2102. https://doi.org/10.1007/s10706-018-0747-9